



TECHNICAL ARTICLE

# Quench Sensitivity of 7475 Aluminum Alloy Using End-Quenching Technique and TTP Diagrams

LIANGHUA LIN <sup>1,2,4</sup> HAIJIAN PENG<sup>1,2</sup> and JUANGANG ZHAO<sup>3</sup>

1.—Jiangxi Engineering Research Center of Process and Equipment for New Energy, East China University of Technology, Nanchang 330013, People's Republic of China. 2.—School of Mechanical and Electronic Engineering, East China University of Technology, Nanchang 330013, People's Republic of China. 3.—School of Material Science and Engineering, Central South University, Changsha 410083, People's Republic of China. 4.—e-mail: linlh@ecut.edu.cn

The quench sensitivity of 7475 aluminum alloy has been comprehensively investigated by hardness testing, electrical conductivity measurements, scanning electron microscopy, and transmission electron microscopy. Based on the end-quenching method and time–temperature–property (TTP) diagram, the key factors affecting the quenching of the studied alloy were identified and are discussed in comparison with other 7000 series alloys. The results indicate that 7475 alloy is relatively sensitive to cooling rate, with a critical temperature range between 300°C and 350°C. The nose temperature of the TTP curve is approximately 330°C, and the incubation period is 1.5 s. When the cooling rate is lower than 12.5°C/s, the density of Guinier–Preston zones and  $\eta'$  precipitates decreases remarkably, and the width of the precipitate-free zone becomes wider. Simultaneously, coarse  $\eta$  phases precipitate at grain/subgrain boundaries and  $\text{Al}_{18}\text{Mg}_3\text{Cr}_2$  dispersoids. These quench-induced  $\eta$  phases consume numerous solute atoms and therefore suppress the formation of the strengthening precipitates, leading to a deterioration of the mechanical properties.

## INTRODUCTION

High-strength 7000 (Al–Zn–Mg–Cu) series aluminum alloys are typical age-hardenable alloys that have been widely used in automotive and aerospace applications. These alloys attain high strength through solution treatment followed by quenching in water and subsequent aging. In general, rapid quenching from the solution treatment temperature is required to achieve supersaturation of solutes and vacancies, which are the prerequisite for the desirable precipitation structure. In contrast, a slow cooling rate will lead to a loss of solutes from the solid solution and a degradation in the mechanical properties. The phenomenon whereby alloys lose their ability to reach the maximum strength as the cooling rate decreases is known as quench sensitivity.<sup>1–3</sup> It is now certain that the quench sensitivity of aluminum alloys plays a critical role in the

service performance of products. For thick plates, the cooling rate decreases from the surface to center layer, which results in inhomogeneity through the thickness.<sup>4,5</sup> From this point of view, reducing the quench sensitivity of the alloy can improve the homogeneity of its microstructure and properties. In addition, for components with complex shapes, a slow quench rate must be adopted to minimize the residual stress or distortion that develops during quenching.<sup>6</sup> Therefore, alloys with low quench sensitivity can achieve adequate properties in most cases.

The end-quenching technique<sup>7</sup> and time–temperature–property (TTP) diagram<sup>8,9</sup> are two effective methods to evaluate the quench sensitivity of high-strength aluminum alloys. The former approach, also known as the Jominy end-quench test,<sup>10</sup> enables the determination of the effect of the quench rate on the microstructure and performance by water spray cooling one end of a cylindrical specimen.<sup>11</sup> Mackenzie and Newkirk proposed that the

end-quenching method can be used to determine the quench factor of aluminum alloys.<sup>12</sup> It has also been utilized to measure the critical cooling rates for AA7N01, 7046A, 7175, 7085, 7075, and 7050 alloys.<sup>7,13–16</sup> This method has also been applied to predict the effects of the quench rate on the mechanical properties of cast aluminum alloy<sup>17</sup> and to quantify the effects of alloying elements on the quench sensitivity.<sup>18–20</sup> The TTP diagram for aluminum alloys is obtained by the interrupted quenching technique, similar to the isothermal time–temperature–transformation curves for steels. From TTP diagrams, it is easy to determine the most critical temperature range for loss in properties, which represents an important parameter describing the quench sensitivity of aluminum alloys.<sup>21</sup> To date, extensive work has been carried out on TTP diagrams of 7000 series alloys.

In particular, 7475 aluminum alloy is a typical high-fracture-toughness alloy of the 7000 series, as this material contains lower amounts of impurity elements such as silicon and iron.<sup>22</sup> One of the major limitations encountered in the application of this alloy is its high quench sensitivity due to the presence of Cr and Mn as minor element additions.<sup>23</sup> To minimize the resulting degradation in properties, as well as to reduce the residual stress and distortion during quenching, step quenching can be used.<sup>24</sup> The principle of this quenching technique is to slowly cool the alloys from the solution treatment temperature to a critical temperature (nose temperature), followed by quenching at a relatively fast rate.<sup>25</sup> Thus, it is of vital importance to determine the quench factors of these alloys. For 7475 aluminum alloy, however, little quantitative data on its quench sensitivity is available yet. Hence, the objective of this work is to determine the key quench factors of 7475 aluminum alloys by using the end-quenching technique and TTP diagrams, paying special attention to a comparison between the studied alloy and some other 7000 series aluminum alloys. The precipitation behavior at different cooling rates is also investigated to reveal the mechanism of quench sensitivity.

## EXPERIMENTAL PROCEDURES

The material used in this study is hot-rolled 7475 aluminum alloy plate with thickness of 25 mm. Its nominal chemical composition (wt.%) is 6.1 Zn, 2.5 Mg, 1.8 Cu, 0.25 Cr, 0.04 Ti, 0.04 Mn, 0.02 Fe, and 0.01 Si, with balance Al. A combination of the end-quenching method and interrupted quenching technique was applied to evaluate the quench sensitivity of the studied alloy. The end-quenching test was performed in accordance with ASTM A255<sup>26</sup> on a custom-designed end-quenching apparatus (Fig. 1). The sample for end-quenching is a 120-mm-long cylinder bar with diameter of 25 mm. The bars were first solution treated at 470°C for 1 h

then rapidly moved to the end-quenching apparatus to undergo water spray cooling. To measure the cooling rate, K-type thermocouples were embedded along the length of the bar. Further details on the measurements can be found in Refs. 11, 13, and 19. After cooling to room temperature, the specimens were divided into two groups. One group was subjected to artificial aging at 120°C for 25 h, whereas the other was not subject to any further treatment. Afterward, the bars were cut at intervals of 10 mm for hardness and electrical conductivity measurements.

To determine the key parameters of the quench sensitivity of the studied alloy, the interrupted quenching method was applied to obtain the time–temperature–property (TTP) curves. Details of this technique are described in Refs. 27 and 28. Specimens with dimensions of  $\Phi 25 \text{ mm} \times 3 \text{ mm}$  were solution heat-treated at 470°C for 1 h, followed by rapid transfer to salt baths at various temperatures ranging from 200°C to 420°C. After isothermal holding for the required duration (1 s to 5000 s), the specimens were water quenched then artificial aged for 25 h at 120°C. Vickers hardness was measured on a HV-10B instrument with load of 2 kg. The electrical conductivity was determined using a D60K digital conductivity meter. At least five electrical conductivity and hardness specimens were measured, and the data reported herein represent average values of the tests.

Microstructural characterization was carried out by transmission electron microscopy (TEM), scanning electron microscopy (SEM), and energy-dispersive x-ray spectrometry (EDS). SEM and EDS observations were carried out on polished samples using a FEI Quanta 200 scanning electron microscope. Samples for TEM were thin discs with diameter of 3 mm, electropolished in 30% nitric acid and 70% methanol solution and cooled to  $-30^\circ\text{C}$  with a voltage of 18 V. Once the specimens were prepared, they were examined using a Tecnai G<sup>2</sup> 20 TEM operating at 200 kV.

## RESULTS AND DISCUSSION

### Time–Temperature–Property (TTP) Curves

The isothermal hardness–time curves of the studied alloy are shown in Fig. 2, revealing that the hardness decreased monotonically with decreasing isothermal hold time for all samples. The rate of decrease of the hardness is determined by the isothermal temperature. In the high temperature range ( $> 420^\circ\text{C}$ ), the hardness drops slowly because of the low degree of undercooling and resultant small driving force for precipitation. When moderate temperatures (300°C to 350°C) are employed, both the degree of undercooling and the diffusion rate of solute atoms are high, thus the hardness decreases dramatically due to the fast precipitation. In particular, the hardness drops most rapidly at 330°C. At temperatures below 250°C, the diffusion

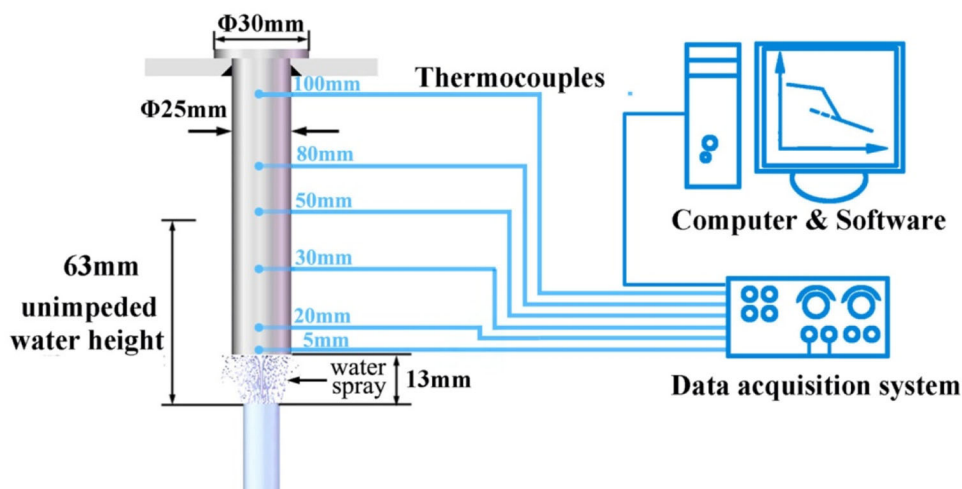


Fig. 1. Schematic drawing of the end-quenching apparatus.

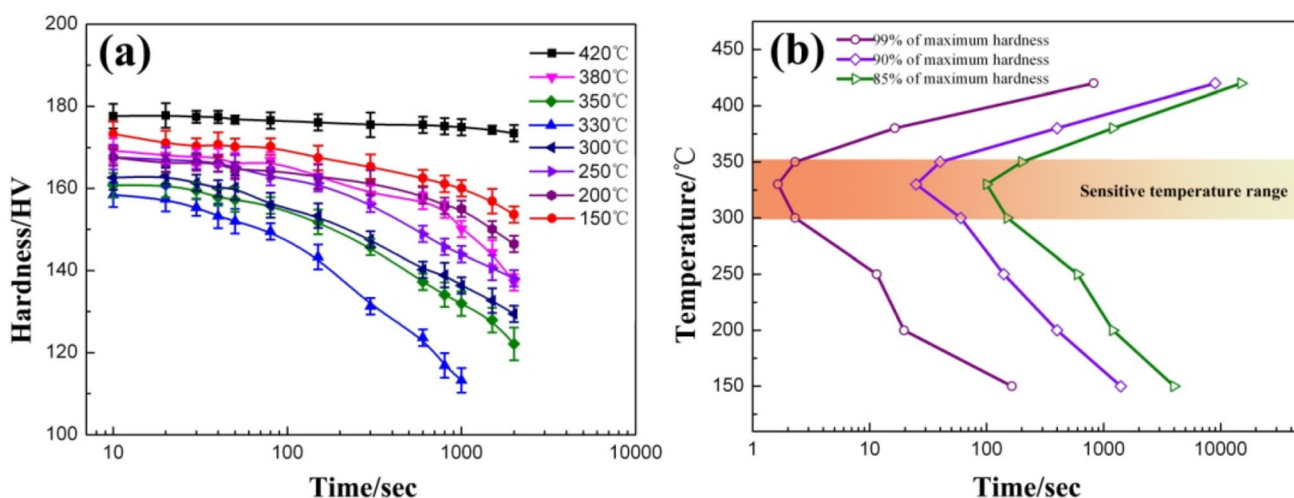


Fig. 2. (a) Effect of isothermal treatment on hardness of 7475 aluminum alloy and (b) TTP diagram.

rate decreases, so the hardness decreases slowly again.

According to the results described above, the TTP curves at 99%, 90%, and 85% of the maximum hardness are plotted in Fig. 2b. It can be seen that the sensitive temperature range is approximately between 300°C and 350°C, which corresponds to the moderate temperature range in Fig. 2a. In this temperature range, the time has a noticeable effect on the mechanical properties of the alloy. Longer holding time in the sensitive temperature range will lead to lower hardness because of the formation of more equilibrium phases.<sup>9</sup> Consequently, it is possible to select a slow cooling rate at the beginning of quenching and then enhance the cooling rate in the sensitive temperature range (300°C to 350°C) to improve the alloy properties.

To further determine the relevant quench sensitivity parameters of the studied alloy, the hardness data in Fig. 2a were fit according to the equation proposed by Evancho and Staley:<sup>29,30</sup>

$$C(T) = -k_1 k_2 \exp \left[ \frac{k_3 k_4^2}{RT(k_4 - T)^2} \right] \exp \left( \frac{k_5}{RT} \right), \quad (1)$$

where  $C(T)$  represents the critical time required to achieve a constant amount of transformation,  $R$  and  $T$  are the gas constant and absolute temperature, respectively,  $k_1$  is a constant which equals the natural logarithm of the fraction untransformed during quenching (typically 0.995),  $k_2$  is a constant related to the number of nucleation sites,  $k_3$  is a constant related to the energy of formation of nuclei,  $k_4$  is a constant related to the solvus temperature, and  $k_5$  is the constant related to the diffusion activation energy. These constants were determined using nonlinear regression analysis. For comparison, the constants of the studied alloy and some other Al-Zn-Mg-Cu alloys available in literature<sup>31-33</sup> are presented in Supplementary Table SI. By using these data and Eq. 1, the TTP

diagrams were constructed and are illustrated in Fig. 3. This figure indicates good agreement between the experimental curve and the fitting result. On these *C*-curves, one key parameter is the “incubation period,” which is related to the stability of the solid solution, and the other parameter is the “nose temperature,” which represents the critical temperature where the hardness decreases rapidly. The quench sensitivity parameters for all the alloys shown in Fig. 3 are presented in Table I. In general, the incubation period corresponds to the onset of quick precipitation.<sup>13</sup> Thus, an alloy with a short incubation period will have high quench sensitivity. For the 7475 alloy, the nose temperature of the TTP curve is approximately 330°C and the incubation period is 1.5 s, suggesting relatively high quench sensitivity. According to the results presented in Table I, the quench sensitivity of these aluminum alloys lies in the following order: 7055 > 7075 > 7475 > 7050 > 7085 > 7A46.

### End-Quenching Test

Figure 4 shows the cooling curves at different distances from the quenched end (named *D*). The temperature at all positions decreases quickly at first, and then slowly until a steady temperature is reached. In this investigation, the average cooling rates are determined by calculating the linear approximation of the slopes between 450°C and 200°C in Fig. 4. It is found that the maximum cooling rate is about 83.3°C/s at *D* = 5 mm. With increasing *D*, the cooling rate gradually decreases. The average cooling rates at 20 mm, 30 mm,

50 mm, 80 mm, and 100 mm from the quenched end are 12.5°C/s, 7.5°C/s, 5.2°C/s, 3.3°C/s, and 2.5°C/s, respectively.

The results for the hardness and electrical conductivity as functions of the distance from the quenched end are presented in Fig. 5 to further illustrate the quench sensitivity of the studied alloy. Note that the electrical conductivity was measured in the as-quenched condition while the hardness was measured in the aged condition. It can be observed from these curves that the electrical conductivity at the quenched end showed the minimum value of 30.5%IACS. When *D* increased from 5 mm to 80 mm (corresponding to cooling rates from 83.3°C/s to 3.3°C/s), the conductivity rapidly increased from 30.5%IACS to 34.3%IACS. It then reached a steady-state value of about 34.6%IACS when *D* was larger than 80 mm. In the as-quenched condition, the electrical conductivity is believed to be associated with the degree of supersaturation of the solid solution while its change reflects the decomposition of the solid solution.<sup>34</sup> Therefore, the fact that the electrical conductivity decreases with the cooling rate is taken as evidence of a drop in the solute concentrations. In addition, the hardness curve shows a progressive decrease as a function of *D*. The maximum value of 175HV is found at the quenched end. It also shows that the percentage hardness reduction is 21% and 34% at the positions *D* = 50 mm and *D* = 100 mm, respectively. The depth of the hardening layer, which is described by the depth corresponding to a 10% drop from the maximum hardness value, is approximately 38 mm. This value is lower than those of

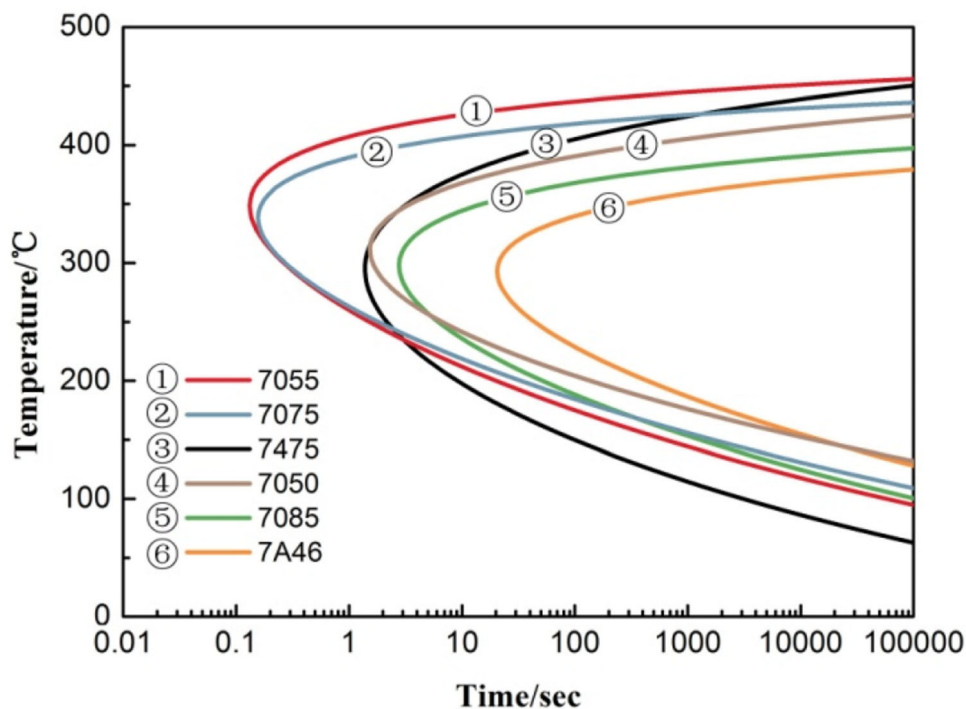


Fig. 3. TTP curves of 7000 series alloys by fitting.

**Table I. Key quench sensitivity parameters for various Al-Zn-Mg-Cu alloys determined by TTP diagrams**

Alloy	Critical temperature range (°C)	Nose temperature (°C)	Incubation period (s)
7475	240–370	300	1.50
7085	260–330	298	3.00
7055	320–380	350	0.15
7A46	265–330	291	21.50
7075	305–370	337	0.17
7050	275–360	310	1.70

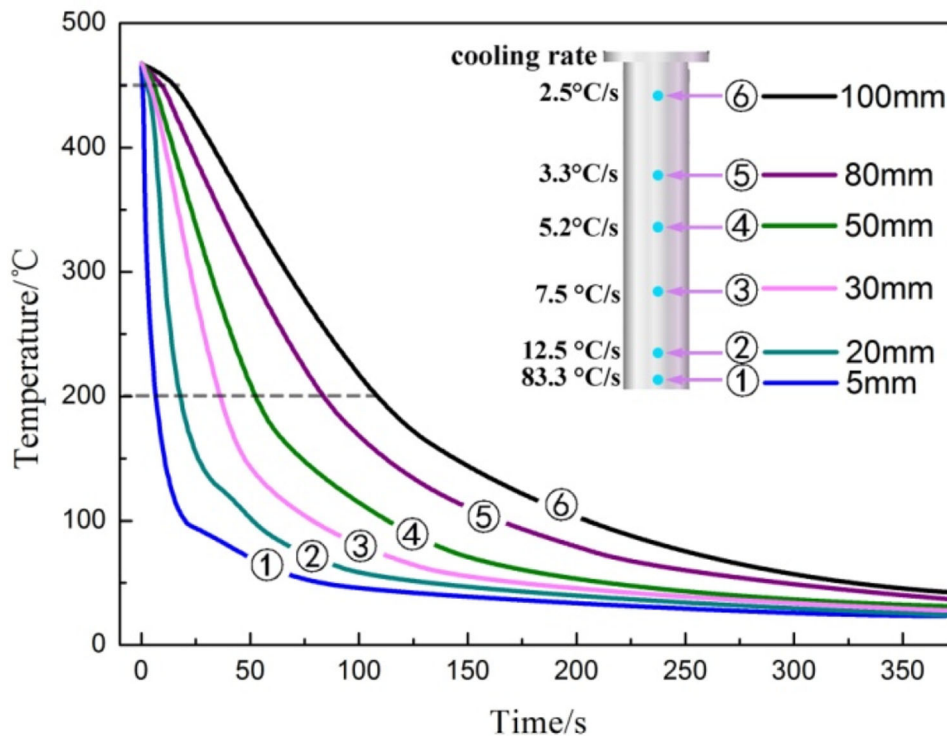


Fig. 4. Cooling curves and cooling rates from end-quenched test. The average cooling rates were determined by the nearly linear temperature range from 450°C to 200°C.

7085 alloy (~ 65 mm),<sup>18</sup> AA7N01 alloy (~ 50 mm),<sup>7</sup> and 7055 alloy (~ 40 mm).<sup>35</sup> Apparently, 7475 aluminum alloy exhibits high quench sensitivity in the light of the relatively low value of the hardening layer depth.

**Microstructural Characterization**

Figure 6 presents the typical SEM microstructure and EDS results of the as-quenched bar at distances of 5 mm and 50 mm. Several large second-phase particles with size of 15 μm to 30 μm are observed at both positions. According to the EDS analysis, these large particles are Fe-bearing and Cr-bearing phases, respectively. Note that these phases are independent of the quenching process, as their sizes and quantities are almost the same at both positions. Therefore, the presence of the second phase has a negligible effect on the quench sensitivity of the alloy. The high-magnification observation in

Fig. 6b reveals a large number of coarse particles distributing along grain boundaries and within the matrix of the alloy at the position of 50 mm. These are readily identified as η equilibrium phases. Compared with Fig. 6b, no obvious equilibrium phase is observed at the distance of 5 mm. Since the cooling rate of the bar decreased with increasing distance from the quenched end, it is obvious that the coarse η equilibrium phases form during slow cooling.

Figure 7 shows typical bright-field TEM images of as-quenched and aged bars at different distances (D = 5 mm, 20 mm, and 50 mm) from the quenched end. In the as-quenched condition, the microstructure at the quenched end shows no coarse η phase along the grain boundaries due to its fastest quench rate, while a few triangular particles and η equilibrium phases are observed in the grain interior, as seen in Fig. 7c. EDS analysis indicates that the

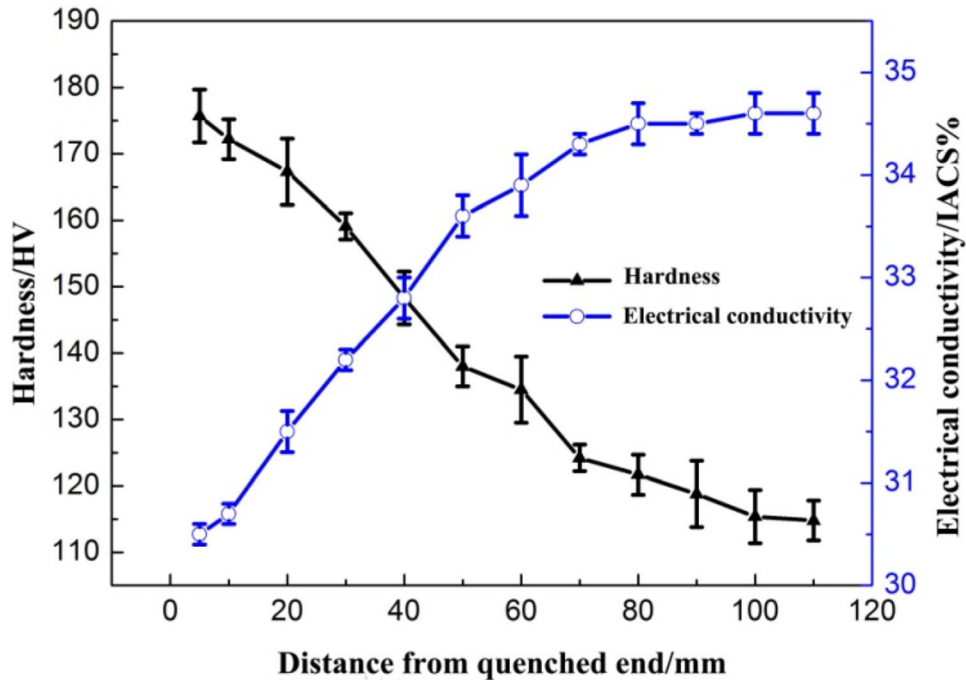


Fig. 5. Hardness and electrical conductivity as functions of distance from the quenched end of the bar.

triangular particles approach  $\text{Al}_{18}\text{Mg}_3\text{Cr}_2$  phase (Supplementary Fig. S1). At the position  $D = 20$  mm, which corresponds to a quench rate of approximately  $12.5^\circ\text{C/s}$ , a few  $\eta$  equilibrium phases with size of 50 nm to 120 nm are distributed along the grain boundaries. With increasing  $D$  (where the quench rate is lower than  $12.5^\circ\text{C/s}$ ), both the number and size of  $\eta$  phase increase significantly. Such  $\eta$  phases on the grain boundary with length larger than 350 nm can be observed at the position  $D = 50$  mm. Obviously, the number and size of the phases at different positions of the sample are controlled by the distance from the quenched end due to the quenching cooling rate. In addition, a noteworthy observation is that the coarse  $\eta$  equilibrium phases primarily precipitate on  $\text{Al}_{18}\text{Mg}_3\text{Cr}_2$  dispersoids, as marked by red arrows in Fig. 7a and d. This result indicates that the Cr-containing dispersoids are the potential nucleation sites for coarse  $\eta$  phases induced by quenching. In general, the grain boundary has high interfacial energy due to their large misfit to the matrix, thereby lowering the energy barrier for precipitation of  $\eta$  equilibrium phase.<sup>35</sup> Likewise, the  $\text{Al}_{18}\text{Mg}_3\text{Cr}_2$  dispersoids also reduce the energy barrier, thus facilitating heterogeneous precipitation on these dispersoids. In Fig. 7, it is apparent that large numbers of coarse  $\eta$  phases nucleated on the preexisting  $\text{Al}_{18}\text{Mg}_3\text{Cr}_2$  particles during slow cooling, which contributes to an increase in the quench sensitivity of the studied alloy.

After aging, a high density of fine precipitates are distributed homogeneously within grains at the quenched end. These dense spherical precipitates

can be identified as GP zones and  $\eta'$  phase according to corresponding selected-area electron diffraction patterns (Supplementary Fig. S2). Meanwhile, large precipitates are continuously distributed along the grain boundaries with narrow precipitate-free zones (PFZs) near the grain boundaries. At the position far from the quenched end, the number density of the precipitates decreases remarkably with a simultaneous increase in the precipitate size, as seen in Fig. 7g, h and i. These changes are caused by the combination of reduction of solute atoms and vacancy concentration due to the reduced quench rate. On one hand, a large number of quench-induced precipitates consumes the considerable amount of solute atoms available to form strengthening precipitates during the subsequent aging process. On the other hand, the quantity of vacancies decreases with decreasing quench rate, causing the diffusion rate of the solute to decrease, and in turn resulting in a low density of GP zones and  $\eta'$  precipitates.

Figure 7 also reveals that the grain boundary precipitates grow significantly, and the width of PFZ becomes wider with decreasing cooling rate. At  $D = 20$  mm (corresponding to a cooling rate of  $12.5^\circ\text{C/s}$ ), the width of PFZ is about 75 nm, while the width increases to 158 nm at  $D = 50$  mm ( $5.2^\circ\text{C/s}$ ). A similar result was also obtained by other authors.<sup>36</sup> The reason for the increase of the PFZ width can be attributed to the vacancy concentration formed at different cooling rates. Since grain boundaries act as sinks for vacancies, there is a concentration gradient of vacancies in the regions near grain boundary. Once the vacancy

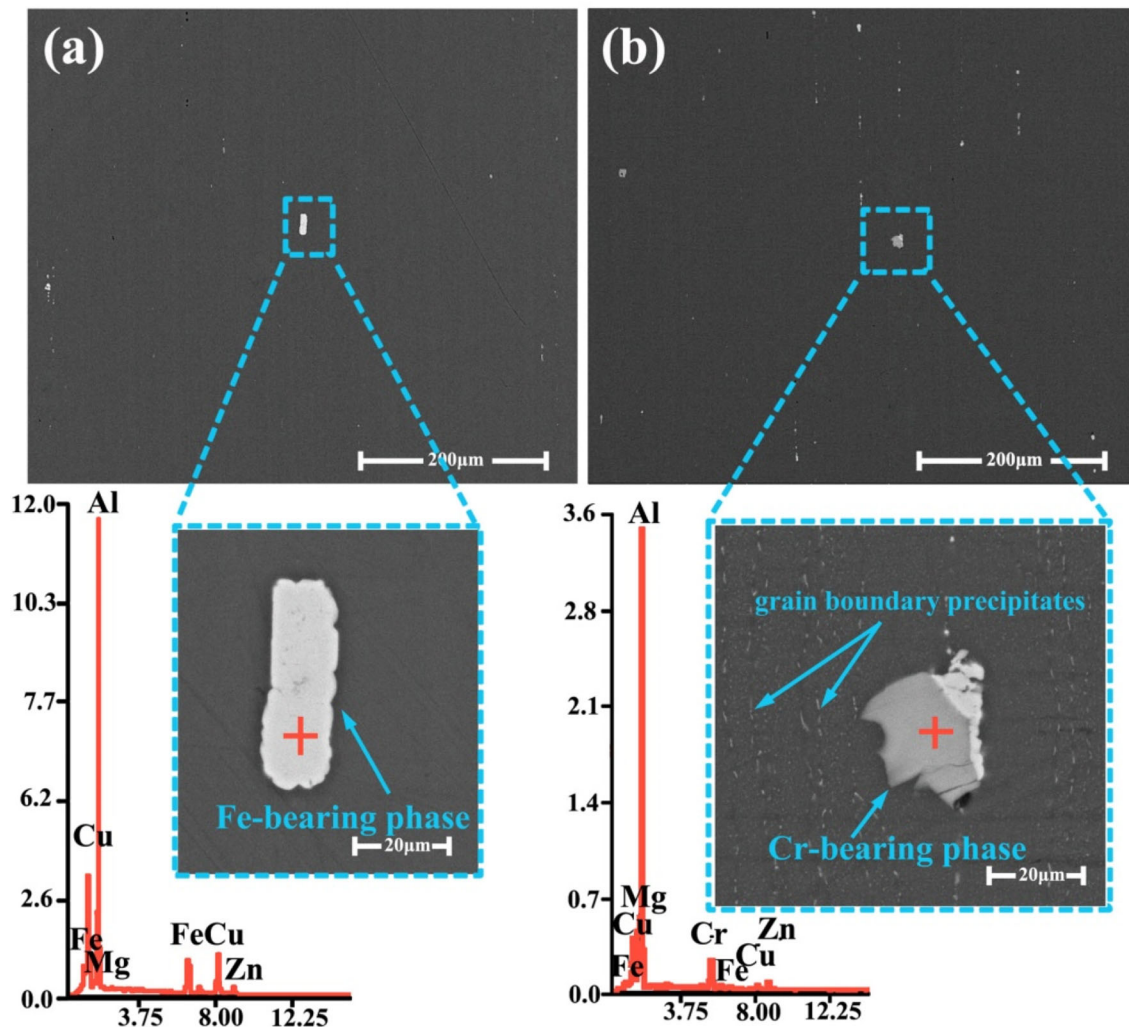


Fig. 6. Typical SEM images and EDS analysis of end-quenched bar at different distances from the quenched end: (a)  $D = 5$  mm, (b)  $D = 50$  mm.

concentration falls below the critical value required for precipitation, PFZ occurs around the grain boundary.<sup>37</sup> In this end-quenching test, the quench rate decreases from 83.3°C/s to 2.5°C/s with an increase in  $D$  from 5 mm to 100 mm. As a result, a wider PFZ forms at the position far from the quenched end as the slower quench rate allows the vacancies to diffuse to the grain boundaries.

In Al-Zn-Mg-Cu alloys, the concentrations of Zn and Mg solutes in supersaturated solid solution is a key factor determining the distribution of fine  $\eta'$  precipitates,<sup>15,18,35</sup> which is the dominant strengthening phase in this series of alloys. From the TEM observations in Fig. 7 and electrical conductivity results in Fig. 5, it is obvious that the precipitation of coarse equilibrium  $\eta$  phase causes the loss of solute elements. Therefore, the microstructure with more coarse  $\eta$  phases at the slow quenching position corresponds to a relatively low degree of supersaturation of solute atoms and the resultant high electrical conductivity. These coarse  $\eta$  phases make

little contribution to the strength of the alloy. They will consume solute atoms nearby and form precipitate-free zones (PFZs) around the coarse phases during aging, as seen in Fig. 7g and h. Similar to PFZ near grain boundary, the PFZ in the vicinity of coarse  $\eta$  phase is relatively soft to the matrix and facilitates stress concentration at this position, thereby further reducing the strength of the alloy.

## CONCLUSION

The quench sensitivity of 7475 aluminum alloy has been investigated by combining the end-quenching method and interrupted quenching technique. The main results can be summarized as follows:

- (1) The depth of the hardening layer of 7475 alloy is about 38 mm. Based on the TTP diagrams, the critical temperature range for the precipitation of  $\eta$  equilibrium phase is between 300°C and 350°C. The nose temperature of the TTP curve is approximately 330°C, and

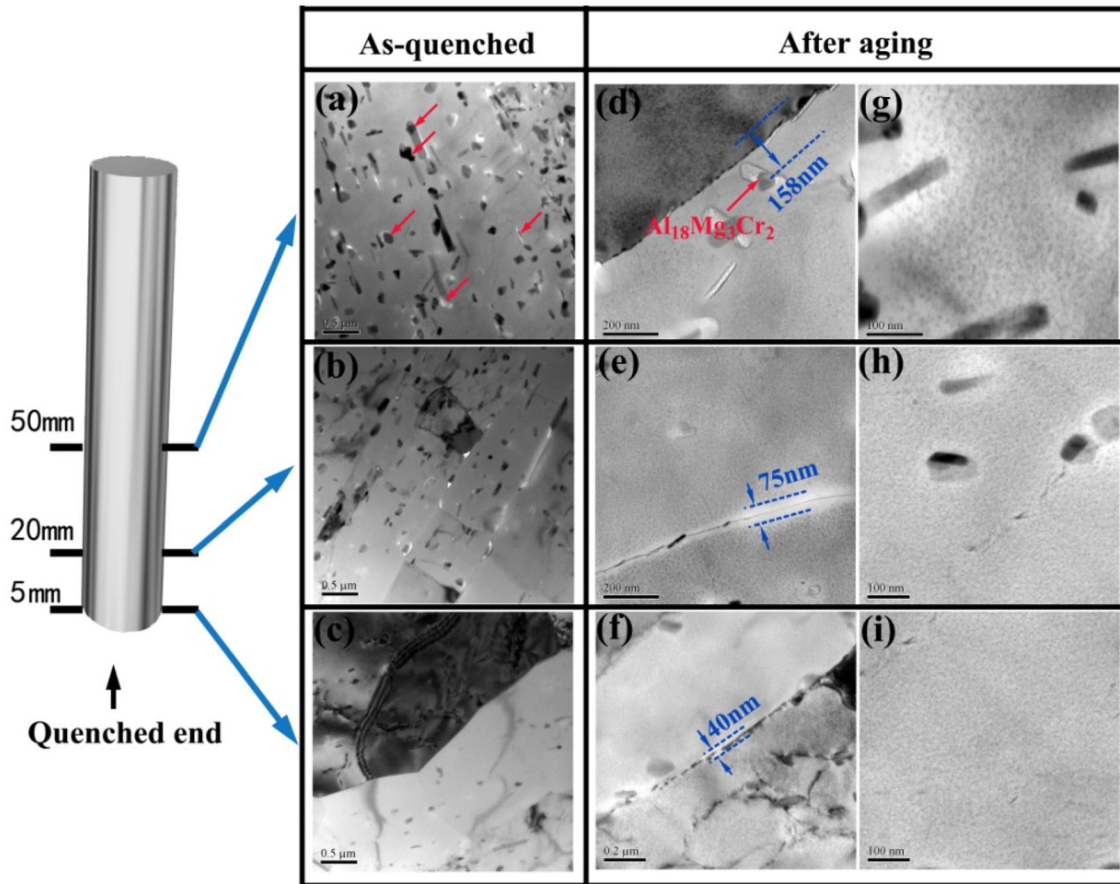


Fig. 7. Typical TEM images of microstructure of end-quenched bar at different distances from the quenched end in (a–c) as-quenched and (d–i) aged condition.

the incubation period is 1.5 s. All these parameters suggest that 7475 alloy is relatively sensitive to cooling rate.

- (2) When the cooling rate is lower than  $\sim 12.5^{\circ}\text{C}/\text{s}$ , the density of GP zones and  $\eta'$  precipitates decreases remarkably and the width of PFZ increases.
- (3) Quenching at a slow rate leads to precipitation of coarse  $\eta$  phases at the grain/subgrain boundaries and  $\text{Al}_{18}\text{Mg}_3\text{Cr}_2$  dispersoids. The quench-induced  $\eta$  phases consume numerous solute atoms and therefore suppress the formation of GP zones and  $\eta'$  precipitates.

#### ACKNOWLEDGEMENTS

This work is financially supported by the Open Project Program of Jiangxi Engineering Research Center of Process and Equipment for New Energy (JXNE2020-06), the East China University of Technology Research Foundation for Advanced Talents (DHBK2017122), and the Scientific Research Project of Jiangxi Education Department (GJJ180409).

#### CONFLICT OF INTEREST

The authors declare that they have no conflict of interest.

#### ELECTRONIC SUPPLEMENTARY MATERIAL

The online version of this article (<https://doi.org/10.1007/s11837-020-04466-0>) contains supplementary material, which is available to authorized users.

#### REFERENCES

1. J.S. Robinson, D.A. Tanner, C.E. Truman, A.M. Paradowska, and R.C. Wimpory, *Mater. Charact.* 65, 73 (2012).
2. M. Tiryakioğlu, J.S. Robinson, and P.D. Eason, *Mater. Sci. Eng., A* 618, 22 (2014).
3. Y. Liu, D. Jiang, B. Li, W. Yang, and J. Hu, *Mater. Des.* 57, 79 (2014).



4. S.T. Lim, S.J. Yun, and S.W. Nam, *Mater. Sci. Eng.*, A 371, 82 (2004).
5. L. Lin, Z. Liu, W. Zhuang, and H. Peng, *Mater. Charact.* 160, 110129 (2020).
6. M.L. Newman, B.J. Robinson, H. Sehitoglu, and J.A. Dantzig, *Metall. Mater. Trans. A* 34, 1483 (2003).
7. H. Xie, Z. Xiao, Z. Li, M. Wang, S. Ma, and H. Jiang, *JOM* 71, 1681 (2019).
8. L. Lin, Z. Liu, S. Bai, P. Ying, and X. Wang, *Mater. Des.* 86, 679 (2015).
9. L. Lin, Z. Liu, S. Bai, Y. Zhou, W. Liu, and Q. Lv, *Mater. Sci. Eng.*, A 682, 640 (2017).
10. M.G.J. 'tHart, H.J. Kolkman, and L. Schra, The Jominy End-Quench Test for the Investigation of Corrosion Properties and Microstructure of High Strength Aluminum. National Aerospace Laboratory, NLR, Netherlands, NLR TR 80102U (1980).
11. S. Liu, C. Li, S. Han, Y. Deng, and X. Zhang, *J. Alloys Compd.* 625, 34 (2015).
12. J.W. Newkirk and D.S. MacKenzie, *J. Mater. Eng. Perform.* 9, 408 (2000).
13. F. Jiang, J. Huang, L. Tang, F. Wang, Q. Xiao, and Z. Yin, *JOM* 71, 1722 (2019).
14. G.P. Dolan, R.J. Flynn, D.A. Tanner, and J.S. Robinson, *Mater. Sci. Technol.* 21, 687 (2005).
15. C. Li and D. Chen, *Metals* 9, 965 (2019).
16. D.S. MacKenzie, *Quench Rate and Aging effects in Al-Zn-Mg-Cu Aluminum Alloys* (Rolla: University of Missouri-Rolla, 2000).
17. S. Ma, M. Maniruzzaman, D.S. MacKenzie, and R.D. Sisson, *Met. Trans. B* 38B, 583 (2007).
18. Y. Deng, L. Wan, Y. Zhang, and X. Zhang, *J. Alloy. Compd.* 509, 4636 (2011).
19. Y.C. Tzeng, C.T. Wu, and S.L. Lee, *Mater. Lett.* 161, 340 (2015).
20. S.K. Chaudhury and D. Apelian, *Int. J. Metalcast.* 10, 138 (2016).
21. R.J. Flynn and J.S. Robinson, *J. Mater. Process. Technol.* 53, 674 (2004).
22. E.A. Starke Jr and J.T. Staley, *Prog. Aeronaut. Sci.* 32, 131 (1996).
23. H.C. Fang, H. Chao, and K.H. Chen, *Mater. Sci. Eng.*, A 610, 10 (2014).
24. B.L. Ou, J.G. Yang, and M.Y. Wei, *Metall. Mater. Trans. A* 38, 1760 (2007).
25. B.C. Shang, Z.M. Yin, G. Wang, and Z.Q. Huang, *Mater. Des.* 32, 3818 (2011).
26. ASTM A255, *Standard Test Methods for Determining the Hardenability of Steel* (West Conshohocken: ASTM, 2014).
27. J.S. Robinson, R.L. Cudd, D.A. Tanner, and G.P. Dolan, *J. Mater. Process. Technol.* 119, 261 (2001).
28. H. Wang, Y. Yi, and S. Huang, *J. Alloys Compd.* 690, 446 (2017).
29. J.T. Staley, *Mater. Sci. Technol.* 3, 923 (1987).
30. J.W. Evancho and J.T. Staley, *Metall. Trans.* 5, 43 (1974).
31. D.J. Chakrabarti, J. Liu, R.R. Sawtell, and G.B. Venema, *Mater. Forum* 28, 969 (2004).
32. S. Liu, Q. Zhong, Y. Zhang, W. Liu, X. Zhang, and Y. Deng, *Mater. Des.* 31, 3116 (2010).
33. J. Ye, Q. Pan, H. Li, Z. Huang, Y. Liu, X. Wang, and M. Li, *JOM* 71, 2054 (2019).
34. G. Waterloo, V. Hansen, J. Gjønnnes, and S.R. Skjervold, *Mater. Sci. Eng.*, A 303, 226 (2001).
35. S. Liu, W. Liu, Y. Zhang, X. Zhang, and Y. Deng, *J. Alloy. Compd.* 507, 53 (2010).
36. D.S. MacKenzie, in *Proceedings from 1st International Symposium on Metallurgical Modeling for Aluminum Alloys* (2003).
37. T. Ogura, S. Hirotsawa, A. Cerezo, and T. Sato, *Acta Mater.* 58, 5714 (2010).

**Publisher's Note** Springer Nature remains neutral with regard to jurisdictional claims in published maps and institutional affiliations.